Remote Sensing of Environment 113 (2009) 2441–2447

Contents lists available at ScienceDirect

Remote Sensing of Environment

journal homepage: www.elsevier.com/locate/rse

Monitoring migration rates of an active subarctic dune field using optical imagery

Marius Necsoiu [a,*], Sébastien Leprince [b], Donald M. Hooper [a], Cynthia L. Dinwiddie [a], Ronald N. McGinnis [a], Gary R. Walter [a]

[a] Geosciences and Engineering Division, Southwest Research Institute® (SwRI®), San Antonio, Texas 78238, United States
[b] Division of Geological and Planetary Sciences, California Institute of Technology, Pasadena, California 91125, United States

ARTICLE INFO

Article history:
Received 27 February 2009
Received in revised form 28 April 2009
Accepted 13 July 2009

Keywords:
Landscape change detection
Optical satellite data
Sand dune migration
Subpixel correlation
Model optimization

ABSTRACT

We developed a novel method to quantify subtle rates of landscape evolution using two satellite imaging systems with different viewing angles and spectral sensitivities. We selected the slowly migrating, high-latitude, subarctic Great Kobuk Sand Dunes (GKSD), Kobuk Valley National Park, Alaska (USA), for our study. The COSI-Corr technique was used for precise orthorectification, co-registration, and subpixel correlation of satellite data. ASTER Visible Near Infrared (VNIR) and SPOT Panchromatic images with a 5-year temporal separation were correlated to measure the horizontal velocity of the GKSD. To reduce correlation noise, ASTER VNIR bands were linearly mixed to match the SPOT Panchromatic band, and raw correlation measurements were projected onto a local robust migration direction to estimate unbiased velocity magnitudes. The results show that the most likely migration rate for the GKSD ranges from 0.5 to 1.5 m/year, with peak velocities up to 3.8 m/year, and uncertainty of approximately 0.16 m/year. The unprecedented ability to measure slow migration rates, including those that may occur over a relatively short time interval, illustrates the value of this method to reliably detect and monitor subtle ground movements including dune migration, glacier flow, mass movements, and other small-scale processes.

1. Introduction

Aeolian atmospheric and geologic systems are highly coupled; in fact, aeolian studies are often undertaken to understand past and potential future climate change (Grove & Warren, 1968; Grove, 1969; Bowler, 1976; Lancaster, 1981; Wells, 1983; Cooke, 1984; Thomas, 1984; Muhs, 1985; Muhs & Moat, 1993; Walker & Barrie, 2006; McGowan et al., 2008; Speirs et al., 2008; Bauer, 2009; Yizhaq et al., 2009). Topography has a strong influence on atmospheric boundary layer dynamics, and the boundary layer controls the initiation of particle lifting into the atmosphere. Aeolian dune forms are controlled by wind regime and sediment supply, and they respond to climate-driven changes in wind circulation. High-latitude, cold-climate dunes are not known to have unique morphologies (Dijkmans and Koster, 1990); however, there is some evidence that such dunes may have significantly lower migration rates than do typical warm, mid-latitude dune systems due, in part, to the presence of movement-arresting niveo-aeolian deposits and/or permafrost at depth (Bourke et al., 2008; Koster and Dijkmans 1988; Mann et al., 2002) and also to the occurrence of opposite, bimodal winds. In this study, the high-latitude (67°N) Great Kobuk Sand Dunes (GKSD), Kobuk Valley National Park, Alaska, USA, were analyzed to test the potential use of optical remote sensing imagery to measure subarctic dune migration rates.

The Co-registration of Optically Sensed Images and Correlation (COSI-Corr) technique (Leprince et al., 2007a,b) has recently proven reliable for measuring dune migration rates (Vermeesch and Drake, 2008). Using pairs of raw pushbroom satellite images, this technique produces pairs of orthorectified images, which are co-registered with accuracy on the order of 1/50 to 1/20 of the pixel size (Leprince et al., 2007a,b). A subpixel correlation algorithm can then be used to estimate local ground displacements between orthorectified image pairs, and typical measurement uncertainty ranges, at 1σ, from 1/10 to 1/5 of the pixel size (Leprince et al., 2007a,b; Ayoub et al., 2008). The COSI-Corr technique was successfully used to automatically compute the sand flux of the world's fastest migrating barchan dunes in Bodélé, Chad (Vermeesch & Drake, 2008), but the uncertainties and limitations of this technique were not completely tested by these authors. They found that the Bodélé dunes were migrating rapidly (up to 200 m/year); therefore, measurement noise was negligible and its estimation warranted only a brief mention (i.e., reported as ~3 m at 1σ). In contrast, the sand dunes selected for our study exhibit much lower migration rates, which may approach, or even be overwhelmed by, the correlation noise.

This paper reports a method based on the COSI-Corr technique, which specifically quantifies the rates of slowly migrating dunes using satellite imaging systems (i.e., ASTER and SPOT) with different viewing angles and spectral sensitivities. To reliably quantify the rates of slowly migrating dunes, we had to overcome two distinct problems, leading to two innovations beyond the standard COSI-Corr technique. First, because the ASTER VNIR and SPOT Panchromatic

* Corresponding author. Tel.: +1 210 522 5541; fax: +1 210 522 5155.
E-mail address: mnecsoiu@swri.org (M. Necsoiu).

0034-4257/$ – see front matter
doi:10.1016/j.rse.2009.07.004

sensors acquire images in different spectral bands, correlating images from these sensors generally leads to noisy measurements (Leprince et al., 2008). Thus, we analyzed the effects of linearly mixing ASTER VNIR bands when correlating ASTER VNIR with the SPOT Panchromatic band, and identified the optimum mixing method in terms of measurement noise. Second, to further reduce the noise and to limit any potential bias to the migration rates derived, we projected the measured horizontal displacement vectors onto a local robust migration direction. The combination of these two innovations was used to characterize the dynamic regime at the GKSD.

This paper is structured as follows: Section 2 reviews the main climatic and geomorphologic characteristics of the study area; Section 3 presents the data and methods used to derive dunes migration rates; Section 4 presents the results, and Section 5 discusses them and concludes the study.

2. Study area

The GKSD occupy an area of 62 km^2 in the central Kobuk River valley, Alaska (Koster & Dijkmans, 1988) (Fig. 1). This active dune system is characterized by a variety of dune forms including transverse, longitudinal, barchanoid, and coppice (nebkha) dunes, as well as sand sheets (Fernald, 1964; Koster & Dijkmans, 1988; Dijkmans & Koster, 1990). Pleistocene glaciation in the Brooks Range produced glacial drift, which was later reworked by subsequent meltwater streams; these streams deposited quartz-rich sand and silt along the axis of the Kobuk River valley concurrent with the last glacial advance occurring 24 ka (Dijkmans & Koster, 1990). Aeolian deposition produced loess and cold-climate dune fields. With the river valley axis oriented east–west, there exists an opposite, bimodal wind regime at the macroscale, whereby the dominant winds are strong polar easterlies approximately 9 months of the year (September–May), but a wind reversal produces westerlies during the summer months (Dijkmans & Koster, 1990).

During the 3-month summer, when winds are from the west, sand is blown upwards on the slip faces of transverse dunes to form 1-m-high secondary lee slopes on the crest lines (Dijkmans & Koster, 1990). Net sand drift is primarily to the west and northwest, as indicated by dune orientations, although summer winds cause minor eastward drift (Brabets, 2001). Dijkmans & Koster (1990) indicated that the paleowind direction responsible for dune formation was from the east (directly east: 90°).

The downwind (west) side of GKSD is characterized by a main body of large transverse to barchanoid (arms pointing downwind to the southwest) dune ridges, longitudinal dunes, and flat interdune areas (Dijkmans & Koster, 1990). The main body of sand is dry with a large sand supply (Dijkmans & Koster, 1990; Mann et al., 2002). Ferrians (1965) suggested that the valley is underlain by discontinuous permafrost in a narrow band immediately surrounding the river but is underlain to the north and south by continuous permafrost at moderately higher elevations including, notably, the area of the GKSD. The potential presence of permafrost within the GKSD combined with the opposite, bimodal wind regime of Kobuk Valley likely leads to slow dune migration (Mann et al., 2002, Necsoiu et al., 2009) when compared with 6–20 m/year migration rates of comparable dunes in typical warm, mid-latitude deserts (Bourke et al., 2008). For example, Yao et al. (2007) calculated dune migration rates of 4.0 to 7.4 m/year, with a mean of 5.3 m/year over a three-decade period for ten transverse, barchan, and barchanoid dunes in the northern Alxa Plateau (Inner Mongolia, China). Also, Long and Sharp (1964) measured the movement of 34 barchan dunes in Imperial Valley, California (USA), between 1941 and 1956 and calculated an average dune migration rate of 15 m/year.

3. Data and methods

In this section, we describe the optical dataset used and briefly review the COSI-Corr technique. Then, we detail the ASTER VNIR band

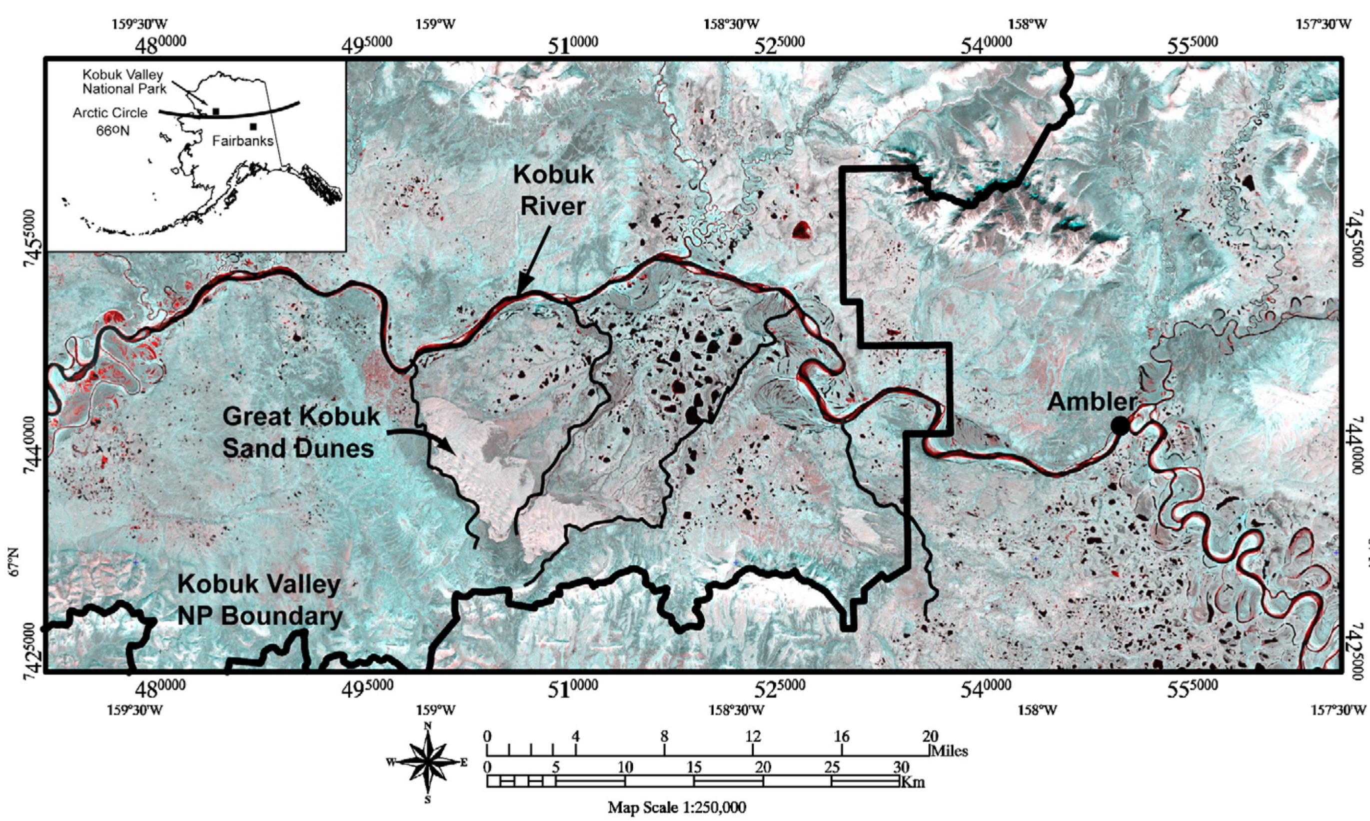

Fig. 1. Location of the Great Kobuk Sand Dunes (GKSD) within Kobuk Valley National Park, AK.

mixing that allows for minimum noise when correlating ASTER VNIR with the SPOT Panchromatic band. Finally, we introduce a method for robust and unbiased estimation of migration rates from horizontal displacement vectors.

3.1. Remote sensing and ancillary data

We used archived satellite data with a 5-year temporal separation (Table 1). Our analysis included a 2.5 m ground resolution SPOT 5 Panchromatic image ($SPOT_{PAN}$) with spectral sensitivities of 0.48–0.71 µm, and 15 m ground resolution ASTER VNIR images with spectral sensitivities of $ASTER_{B1}$ (0.52–0.60 µm), $ASTER_{B2}$ (0.63–0.69 µm), and $ASTER_{B3N}$ (0.76–0.86 µm) (Fig. 2).

Existing geomorphologic and lithologic maps of the GKSD (Dijkmans & Koster, 1990; KOVA, 2001; Mann et al., 2002) were essential in the selection process of representative aeolian sand deposits (Fig. 3a). Fig. 3b depicts the active dune fields, stabilized sand sheets and partly stabilized dunes, as mapped in outline by KOVA (2001).

3.2. Orthorectification, co-registration and subpixel correlation

The COSI-Corr technique described in Leprince et al. (2007a) was used to accurately orthorectify, co-register, and correlate ASTER and SPOT imagery. Satellite data were processed as follows (Necsoiu et al., 2009):

1. A 15-m DEM was generated using the ASTER stereoscopic views 3N/3B.
2. The SPOT L1A Panchromatic image was orthorectified at a resolution matching the ASTER VNIR resolution of 15 m.
3. The ASTER L1A VNIR bands were orthorectified by selecting 15 tie points, outside the active dune field, between the raw ASTER and the orthorectified SPOT images. These tie points were used to generate optimized ground control points (GCP) through correlation analysis, ensuring accurate co-registration between SPOT and ASTER orthorectified images. Three GCPs had high residual values and were eliminated. All ASTER VNIR bands were sequentially orthorectified using the same procedure.
4. The co-registered and orthorectified datasets were correlated using phase correlation to estimate horizontal displacement in east/west (E/W) and north/south (N/S) directions. To assess the quality of results, a signal to noise ratio (SNR) image, as defined in Leprince et al. (2007a), was computed. To discard any potential outliers, measurements not within ± 30 m offset in both N/S and E/W direction, or with an SNR lower than 0.9, were eliminated.
5. Finally, all correlation results were destriped to suppress attitude residuals from the ASTER platform (Leprince et al., 2007b; Scherler et al., 2008; Ayoub et al., 2008). For consistency, all correlations used the same destriping model.

3.3. Correlating panchromatic SPOT and VNIR ASTER data

Previous studies (Ayoub et al., 2008; Vermeesch & Drake, 2008; Scherler et al., 2008) used only the $ASTER_{B3N}$ band in the correlation process. When no spectral limitations are present (i.e., when correlating ASTER datasets together), this band usually offers the best SNR because it has the largest spectral bandwidth, if we assume uniform sunlight power in each ASTER VNIR band. However, when correlating ASTER VNIR with SPOT Panchromatic data (i.e., $SPOT_{PAN}$), there is no spectral overlap between the $ASTER_{B3N}$ and $SPOT_{PAN}$ bands (Fig. 2). To limit the effects of reflectivity differences between the images to be correlated, we studied the influence of linearly mixing ASTER VNIR bands (Table 2) on correlation noise and outliers. Eight methods were tested:

M1. Correlation of $ASTER_{B1}$ and $SPOT_{PAN}$ orthoimages.

M2. Correlation of $ASTER_{B2}$ and $SPOT_{PAN}$ orthoimages.

M3. Correlation of $ASTER_{B3N}$ and $SPOT_{PAN}$ orthoimages.

M4. Correlation of $ASTER_{PAN\text{-}2}$ and $SPOT_{PAN}$ orthoimages. The $ASTER_{PAN\text{-}2}$ image was generated by averaging the first two ASTER bands:

$$ASTER_{PAN-2} = 0.5 \times ASTER_{B1} + 0.5 \times ASTER_{B2} \quad (1)$$

M5. Correlation of $ASTER_{PAN\text{-}2W}$ and $SPOT_{PAN}$ orthoimages. The $ASTER_{PAN\text{-}2W}$ image is the linear mixing of the $ASTER_{B1}$ and $ASTER_{B2}$ orthoimages that best approximate the $SPOT_{PAN}$ orthoimage, in the least squares sense. Specifically, we determined α and β that minimized:

$$\sum [\beta(\alpha \times ASTER_{B1} + (1-\alpha) \times ASTER_{B2}) - SPOT_{PAN}]^2 \quad (2)$$

over the area where ASTER and SPOT orthoimages overlap. β represents a linear contrast stretch between SPOT and ASTER data and is therefore not explicitly solved for. Indeed, the normalized phase correlation algorithm used is insensitive to linear contrast stretch (Leprince et al., 2007a), and this parameter has no influence on our correlation analysis. Solving Eq. (2), we found:

$$ASTER_{PAN-2W} = 0.43 \times ASTER_{B1} + 0.57 \times ASTER_{B2}. \quad (3)$$

The $ASTER_{PAN\text{-}2W}$ image can be seen as a simulated “Panchromatic” ASTER band that best matches the SPOT Panchromatic band, minimizing the reflectivity differences between ASTER and SPOT images. This method of determining the $ASTER_{PAN\text{-}2W}$ image is also a more rigorous solution to method 4, which used a more intuitive approach for mixing ASTER bands. It is possible to rigorously generate an ASTER “Panchromatic” image because all data involved in Eq. (2) are well co-registered. For this reason, we used the produced orthoimages co-registered with subpixel accuracy, rather than the raw images that are not geometrically rectified, nor registered. Theoretically, Eq. (2) should only be solved for pixels that have not sustained any ground motion. In practice, we used all the overlapping pixels in the images, including the pixels from the active dunes for two reasons. First, because the GKSD have slow migration rates, expected motions are within the pixel size. Hence, for radiometric matching, potential bias seems negligible. Second, the active dune area is the only area in the images having high radiometric values. Therefore, for Eq. (2) to constrain most of the radiometric range, all image pixels were included in our matching computation.

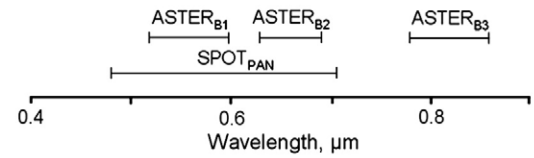

Fig. 2. Spectral bandwidth for ASTER and SPOT bands used in this study.

Table 1
Optical datasets used in this study.

Satellite dataset granule ID	Acquisition date	Viewing angle	Orientation (°)
ASTER L1A#00306142003222530	6/14/2003	−0.025	21.2405
SPOT 5 K/J 421-210/6	8/7/2008	−15.41	18.7687

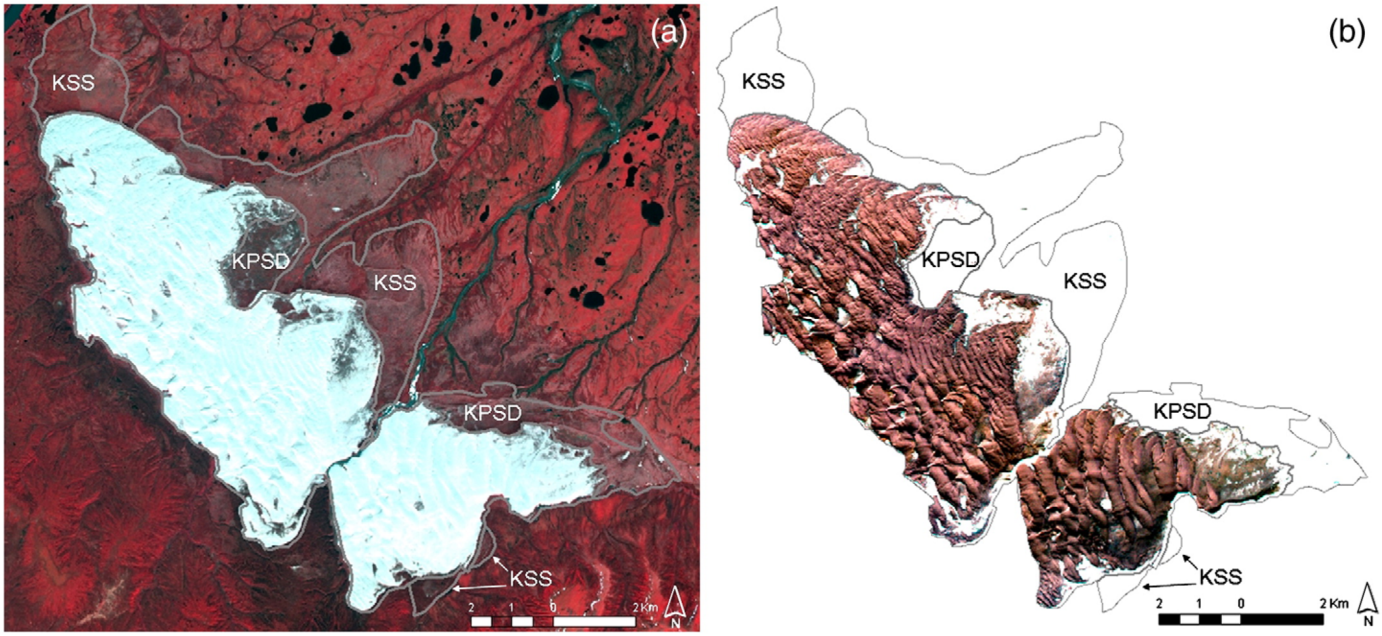

Fig. 3. (a) ASTER (3N, 2, 1) color composite showing the GKSD and surrounding area. (b) The GKSD active dunes are pictured with a contrast-enhanced ASTER (3N, 2, 1) image (maroon). Grey outlines delineate the lateral extent of the stabilized sand sheet (KSS) and Kobuk partly stabilized dunes (KPSD).

M6. Correlation of $ASTER_{PAN\text{-}3W}$ and $SPOT_{PAN}$ orthoimages. The $ASTER_{PAN\text{-}3W}$ image was generated as in method 5, but extended to all three ASTER VNIR bands. After solving Eq. (2) for a three-band formulation, we obtained:

$$ASTER_{PAN-3W} = 0.25 \times ASTER_{B1} + 2.4 \times ASTER_{B2} - 1.65 \times ASTER_{B3N} \quad (4)$$

M7. Average of the correlation results from methods 1 and 2.

M8. Average of the correlation results from methods 1, 2, and 3.

Eqs. (3) and (4) reveal that the dominant component is the $ASTER_{B2}$ band. Eq. (4) also reveals that $ASTER_{B3N}$, which lies outside the $SPOT_{PAN}$ spectral range, has a negative coefficient, showing an anti-correlation with other bands in terms of radiometry.

For each method, we estimated the correlation noise by selecting regions of stabilized sand sheets (KSS, Fig. 3) that had a reduced movement. The best method was selected based on a) the lowest displacement standard deviation within the selected stable areas, and b) the fewest number of discarded measurements (i.e., outliers) over the whole image. Results are reported in Table 2.

Table 2
Influence of ASTER VNIR band mixing on correlation noise and outliers, when ASTER VNIR and SPOT Panchromatic images are correlated.

	Method	Noise sigma (m)		Decorrelation (%)
		E/W	N/S	
1	ASTERB1 vs. SPOTPAN	1.16	0.78	5.26
2	ASTERB2 vs. SPOTPAN	1.12	0.81	4.13
3	ASTERB3N vs. SPOTPAN	5.18	4.82	16.56
4	ASTERPAN-2 vs. SPOTPAN	1.07	0.70	4.45
5	ASTERPAN-2W vs. SPOTPAN	1.07	0.70	4.39
6	ASTERPAN-3W vs. SPOTPAN	2.00	2.05	31.02
7	ASTER_SPOTSTACK-2 i.e., 0.5×(ASTERB1 vs. SPOTPAN)+ 0.5×(ASTERB2 vs. SPOTPAN)	1.07	0.69	5.45
8	ASTER_SPOTSTACK-3 i.e., 1/3×(ASTERB1 vs. SPOTPAN + ASTERB2 vs. SPOTPAN + ASTERB3N vs. SPOTPAN)	4.02	3.95	12.22

Methods 1 and 2 can be seen as the best "single-band" methods, where an overlapping spectral band from the ASTER sensor is correlated with the SPOT Panchromatic band (Table 2). Both methods produced similar noise levels, although method 2 produced fewer outliers. This observation is consistent with the fact that the $ASTER_{B2}$ band is the dominant component of Eq. (3); the SPOT Panchromatic band "looks" more like $ASTER_{B2}$ than $ASTER_{B1}$.

Whenever the $ASTER_{B3N}$ band was used (i.e., methods 3, 6, and 8), the correlation showed large levels of noise and decorrelations (i.e., outliers). The $ASTER_{B3N}$ and $SPOT_{PAN}$ bands do not overlap, and the images to be correlated do not look alike. Hence, not surprisingly, methods 3, 6, and 8 present the largest percentage of decorrelation and are not suitable for accurate correlation analysis.

If we only analyze the standard deviation results, we might conclude that methods 4, 5, and 7 are the best, and are equivalent. By linearly combining $ASTER_{B1}$ and $ASTER_{B2}$, methods 4 and 5 produce images with reduced radiometric noise and higher SNR. Thus, methods 4 and 5 offer a lower level of correlation noise than methods 1 and 2. It is also interesting to note that method 7 offers the same noise level as methods 4 and 5, although the noise reduction process is different. The correlation noise between methods 1 and 2 are mostly uncorrelated and noise reduction occurred when averaging the results from both methods. However, method 7 produced significantly more outliers than methods 4 and 5. This is because outliers from $ASTER_{B1}$ vs. $SPOT_{PAN}$ and from $ASTER_{B2}$ vs. $SPOT_{PAN}$ do not occur at the same location, and thus more outliers are produced when averaging these correlations. Indeed, when a valid measurement is averaged with an outlier, another outlier is created. The same effect, leading to the same conclusion, also occurred when using method 8.

Overall, the results also show that the E/W noise component was larger than the N/S noise component.

We finally selected the $ASTER_{PAN\text{-}2W}$ vs. $SPOT_{PAN}$ correlation method 5 for estimating the migration rates of the active GKSD because it offers the smallest noise level, and produces fewest outliers, thus providing more valid measurements.

3.4. Velocity calculation

According to Leprince et al. (2007a), the noise on each E/W and N/S component of the correlation can be modeled as additive white Gaussian noise. If X and Y are portrayed as two independent random variables following a normal distribution with variance σ^2, then the magnitude given by $\sqrt{X^2+Y^2}$ will follow a Rayleigh distribution with mean $\mu=\sigma\sqrt{\pi/2}$ (e.g., Meikle, 2001). Thus, if we were to estimate the displacement magnitude of the dune field by computing the Euclidean norm of the E/W and N/S components, it would be overestimated by a quantity close to μ. The potential mean bias would then be approximately 1.25 m (or 0.24 m/year in this context), if we assume the standard deviation of the noise to be approximately 1 m for the selected correlation method (Table 2). In our case, the displacement magnitude is so close to the noise level that our estimates could be significantly biased. Unbiased estimates of the displacement magnitudes can be obtained if we instead project each displacement vector onto a robust local migration direction that is independent of the noise. The projected measurements then have the advantage of preserving the original noise characteristics, i.e., zero mean and white Gaussian noise. The local robust migration direction is defined as the unitary vector $u=(\cos(\theta), \sin(\theta))$ that robustly represents the local migration orientation θ. For each measurement, u is determined as follows:

1. Compute the noisy measurement direction vector:

$$\cos(\theta_i)=d_{EW}/\sqrt{d_{EW}^2+d_{NS}^2}, \quad \sin(\theta_i)=d_{NS}/\sqrt{d_{EW}^2+d_{NS}^2} \tag{5}$$

2. Determine the median of each component of the noisy direction vector:

$$Mc=Median\{\cos(\theta_i)\}, \quad Ms=Median\{\sin(\theta_i)\} \tag{6}$$

3. Deduce the robust direction unitary vector:

$$\cos(\theta)=Mc/\sqrt{Mc^2+Ms^2}, \quad \sin(\theta)=Ms/\sqrt{Mc^2+Ms^2} \tag{7}$$

where

d_{EW} E/W displacement measured from correlation
d_{NS} N/S displacement measured from correlation
θ_i Migration orientation corresponding to the (d_{EW}, d_{NS}) vector measurement.

For each measurement, the median operation was defined over the 5×5 neighboring measurements. The median filter window size was small enough to confidently sample the complexity of the area, yet large enough to have statistical meaning. The displacement magnitudes were then estimated as follows:

$$Displ\_mg=d_{EW}\times\cos\theta+d_{NS}\times\sin\theta \tag{8}$$

where

d_{EW} and d_{NS} are defined as in Eqs. (5)–(7)

$u=(\cos(\theta), \sin(\theta))$ is the robust local migration direction deduced from Eq. (7).

Migration rates were simply derived by dividing the displacement magnitudes by the time elapsed between images (1881 days, or ~5.15 years).

4. Results

Fig. 4 presents the velocity field over the active dune area. It shows that (1) there is a very strong west–northwest orientation of sand movement

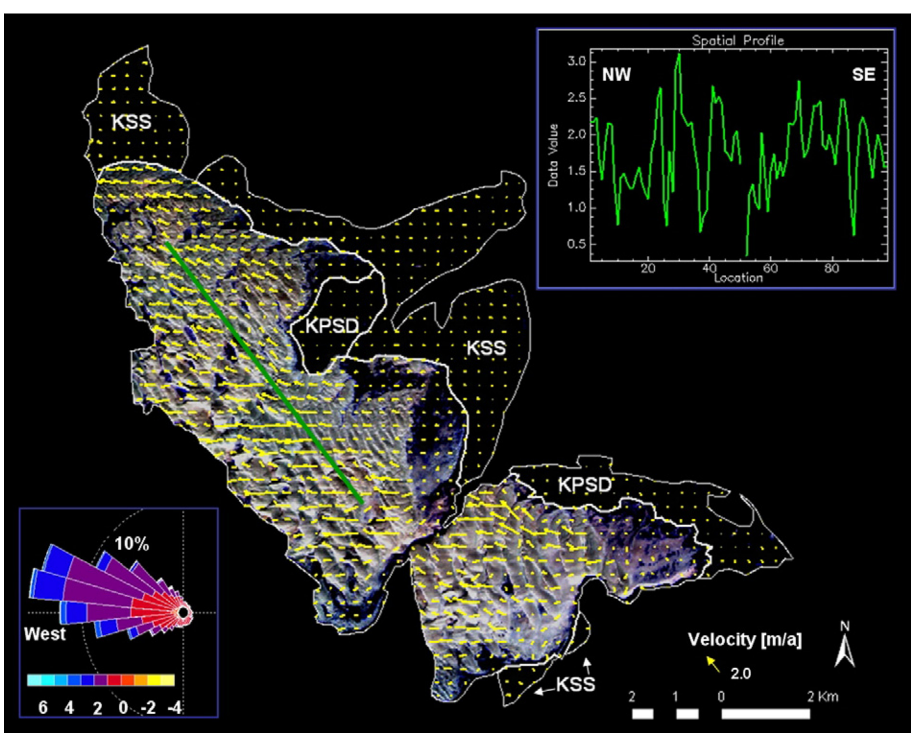

Fig. 4. Calculated velocity field around the GKSD. The green transect shows the area with maximum migration rates; KSS is stabilized sand sheet and KPSD is Kobuk partly stabilized dunes. The rose diagram show wind distribution over the entire active dune field. Background image: contrast-enhanced SPOTPAN image.

related to the dunes; (2) this trend immediately becomes more scattered, nondirectional, or random outside the zone of active sand dunes; (3) subregions dominated by flat interdune corridors, deflation, and sand sheets (rather than transverse or barchanoid dunes) appear to have less movement or a smaller magnitude of calculated flux (an anticipated result); and (4) in the far-eastern section of the GKSD, where we suspected some deflation, a northward rather than a west–northwest direction was estimated. This region is predominantly a sand sheet and stabilized dunes.

A transect across recognizable dune forms over areas having relatively large migration rates revealed velocities on the order of 2 m/year (Fig. 4). However, the mean velocity along this transect is 1.28 m/year with an uncertainty of 0.78 m/year at 1σ. Fig. 5 shows the probability density of the velocity measurements over active and stable sand dunes. Active areas have a calculated mean velocity of 1.15 m/year. However, examining the shape of the density plot reveals that the most likely migration rate estimate is between 0.5 and 1.5 m/year, with peak velocities up to 3.8 m/year. Stable areas revealed a mean velocity of 0.20 m/year $\pm$ 0.16 m/year at 1σ, and uncertainty can be used to characterize the measurement noise. It is interesting to note that the noise density is approximately Gaussian, symmetrical, and does not have a Rayleigh-like shape. This was an expected result because the measurements were projected onto a local robust migration direction. The shape of the velocity probability density over stable areas offers evidence that our method provides unbiased measurements. The negative velocity measurements are not physical; rather, they correspond to areas where Gaussian noise exceeds velocity. If the stable areas were indeed not migrating, only noise should be measured and mean velocity should be zero. The mean velocity over stable areas is not exactly zero and the migration direction over these areas is not entirely random, but seems to be oriented with the prevailing wind direction. We hypothesize that the "stable" areas selected for our tests were not completely stable, but are actually migrating at a very slow rate of approximately 0.2 m/year.

5. Discussion and conclusion

This study proposes an extension to the conventional approach (Vermeesch & Drake, 2008) of using optical imagery to monitor migration rates of dune fields. Our research showed that the $ASTER_{PAN-2W}$ vs. $SPOT_{PAN}$ correlation method is the best choice when pairs of ASTER and SPOT images are analyzed. Such linear mixing between VNIR bands $ASTER_{B1}$ and $ASTER_{B2}$ had two consequences:

1. It increased the SNR of the mixed image by reducing radiometric noise, and thus decreased the measurement noise on valid measurements;

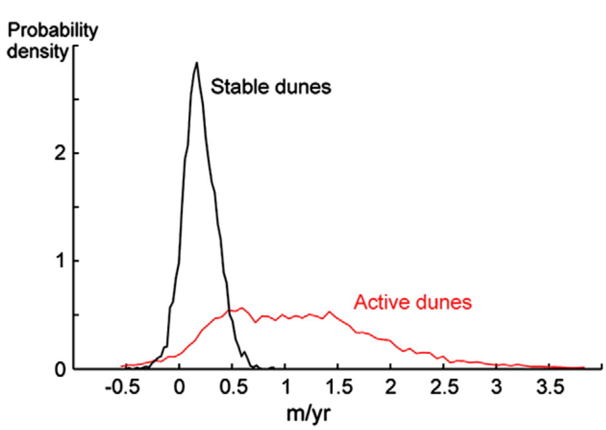

Fig. 5. Probability density of the velocity measurements over active and stable GKSD sand dunes. The negative values are a consequence of the projection operator, as the noise is kept Gaussian in this representation.

2. It reduced the amount of decorrelation by comparing images that look more similar, and thus produced more valid measurements.

While a similar effect to the first consequence was also observed when correlation results were averaged, the opposite of the second consequence was observed with the averaging method because it combined all outliers from both correlations (cf., method 7). As a corollary to these two consequences, we more generally learned that:

1. Decreasing the radiometric noise on the images to be correlated reduces correlation noise;
2. Correlating images acquired from matching spectral bands reduces the amount of decorrelation areas, or outliers, in the correlation results.

The selected $ASTER_{PAN-2W}$ vs. $SPOT_{PAN}$ correlation method best matches the radiometry, but does not influence the geometry. Therefore, if attitude residuals were to be noticed between the ASTER spectral bands, linear mixing of the spectral bands would not be accurate because mis-registered pixels would be mixed together. In our study, we did not find any attitude differentials between ASTER bands, allowing the proposed band mixing to be radiometrically and geometrically accurate. Indeed, the correlation $ASTER_{B1}$ vs. $ASTER_{B2}$ showed no differential attitude. We acknowledge that this verification is necessary as this result might not hold in general. We also noticed that if a simpler method to correlate ASTER and SPOT images were to be sought, the $ASTER_{B2}$ vs. $SPOT_{PAN}$ method produced acceptable results (Table 2). In addition, if the rigorous method 5 proposed cannot be performed due to, for instance, large displacement between the objects to be matched, a "blind" mixing by simply averaging the bands $ASTER_{B1}$ and $ASTER_{B2}$ produced the second-best results (see method 4, Table 2).

The implementation of the COSI-Corr method confirmed two issues previously published in Leprince et al. (2007a) and Scherler et al. (2008): (1) if data are affected by attitude residuals, this will bias the measurement direction and amplitude, making it necessary to destripe the E/W and N/S displacements before calculating the displacement field, and (2) topographic bias: if the topography is not well-resolved by the DEM, or if the topography changes between acquisitions (e.g., because the dunes are moving) and this change is not reflected in the DEM, a horizontal displacement bias, mostly E/W oriented (i.e., in the epipolar direction), will occur. This may be the reason why our results show higher E/W than N/S standard deviations. Our current inability to confirm the quality of the ASTER DEM data, coupled with a high incidence angle between the datasets, is potentially the largest source of bias in this study.

We investigated a velocity estimation approach where raw measurements were projected onto a local robust migration direction. Because the raw E/W–N/S measurement noise is modeled as additive, white, and Gaussian, the derivation of velocity via the Euclidean norm would be overestimated. In addition, because the projected velocity measurements become only sensitive to the local migration direction, noise filtering naturally occurs. Indeed, the noise component perpendicular to the migration direction is automatically filtered out, further reducing the noise on the velocity measurements. Although we observed nonphysical negative velocities, which should be regarded as noise only, we produced reliable and unbiased measurements of slowly migrating sand dunes. We achieved a level of noise of approximately 0.16 m/year (absolute unit 0.82 m, or ~1/18 of the pixel size). This result is to be compared to similar studies where SPOT and ASTER images were correlated to achieve at best a noise standard deviation of approximately 1.3 m, equivalent to ~1/11 of the pixel size (Leprince et al., 2008). By examining the density plot of the estimated velocities, we concluded that the most likely migration rate for the GKSD is between 0.5 and 1.5 m/year, with a mean velocity of 1.15 m/year, and peak velocities up to 3.8 m/year.

Bourke et al. (2008) recently reported a Victoria Valley, Antarctica, 1.5 m/year average dune migration rate estimate over a 40-year period for perennial niveo-aeolian transverse and barchan sand dunes. In contrast, niveo-aeolian deposits at the GKSD are ephemeral, disappearing each summer, which suggests they would play a lesser role in arresting dune movement; however, movement-limiting permafrost is suspected at depth within the GKSD (Koster & Dijkmans, 1988; Mann et al., 2002). Our 1.15 m/year average migration rate estimate over a 5-year period for the active GKSD dunes is thus consistent with the Antarctica estimate given similarities in dune morphology and size.

The methodology applying the COSI-Corr technique, multispectral information, orientation filtering, and orientation projection, allowed reliable measurement of slowly migrating sand dunes. It is a fast and economically viable method that can provide accurate results for detecting and monitoring active morphological processes, subtle ground movements, glacier flow/mass movements, and other processes that affect optical data patterns.

Acknowledgements

SwRI® researchers were funded through SwRI's internal research and development program, Quick-Look Project R8002: Kobuk Valley National Park Landscape Change Detection Using Remotely Sensed Data and Geomorphologic Assessments. S. Leprince was partially supported by NSF grant EAR-0636097, and by the Gordon and Betty Moore Foundation. The background image of Fig. 1 is a composite of two Landsat datasets (Path 078; Row 013, 2002/08/30, 1985/07/06), courtesy of Global Land Cover Facility. ASTER dataset courtesy of NASA LP-DAAC, USGS and Japan's METI. SPOT Panchromatic dataset was acquired from SPOT Image Inc. We greatly appreciate the constructive comments of the anonymous reviewers and P. Vermeesch for his insightful review and suggestions. We thank E. Beverly for data reduction, A. Morris and D. Ferrill for their technical and programmatic reviews, L. Mulverhill for editorial review, and C. Patton her assistance with formatting this manuscript.

References

Ayoub, F., Leprince, S., Binet, R., Lewis, K., Aharonson, O., & Avouac, J. P. (2008). Influence of camera distortions on satellite image registration and change detection applications. *Proc. IGARSS, Boston, MA, USA, July 2008*.

Bauer, B. O. (2009). Contemporary research in aeolian geomorphology. *Geomorphology*, *105*, 1−5.

Bourke, M. C., Ewing, R., Finnegan, D., & McGowan, H. A. (2008). Migration rates of niveo-aeolian dunes in Antarctica: Implications for Martian dunes. *Planetary Dunes Workshop: A Record of Climate Change, 29 April–2 May 2008, Abstract #7040, Alamogordo, New Mexico*.

Bowler, J. M. (1976). Aridity in Australia: Age, origins and expression in aeolian landforms and sediments. *Earth Science Reviews*, *12*, 279−310.

Brabets, T. P. (2001). Hydrologic data and a proposed water-quality monitoring network for the Kobuk River basin, Gates of the Arctic National Park and Preserve, and Kobuk Valley National Park, Alaska. *USGS Water-Resources Investigations Report 01-4141* Available at: pubs.usgs.gov/wri/wri014141/

Cooke, H. J. (1984). The evidence from northern Botswana of late Quaternary climate change. In J. C. Vogel (Ed.), *Late Cainozoic palaeoclimates of the southern hemisphere* (pp. 265−278). Rotterdam: Balkema.

Dijkmans, J., & Koster, E. (1990). Morphological development of dunes in a subarctic environment, central Kobuk valley, northwestern Alaska. *Geografiska Annaler*, *72A*, 93−109.

Fernald, A. T. (1964). Surficial geology of the central Kobuk River valley, northwestern Alaska. *USGS Bulletin*, *1181-K*, k1−k31.

Ferrians, O.J. Jr. (1965). Permafrost map of Alaska. USGS Miscellaneous Geologic Investigations Map I-445, scale 1:2,500,000.

Grove, A. T. (1969). Landforms and climate change in the Kalahari and Ngamiland. *Geographical Journal*, *135*, 190−212.

Grove, A. T., & Warren, A. (1968). Quaternary landforms and climate on the south side of the Sahara. *Geographical Journal*, *134*, 189−208.

Koster, E. A., & Dijkmans, J. W. A. (1988). Niveo-aeolian deposits and denivation forms, with special reference to the Great Kobuk Sand Dunes, Northwestern Alaska. *Earth Surface Processes and Landforms*, *13*, 153−170.

KOVA (2001). Ecological Subsections of Kobuk Valley National Park, NPS, GIS Data (ESRI Shapefile) and Metadata Available at: nrdata.nps.gov/kova/kovadata/subse_ko.zip

Lancaster, N. (1981). Palaeoenvironmental implications of fixed dune systems in southern Africa. *Palaeogeography, Palaeoclimatology, Palaeoclimatology*, *33*, 327−346.

Leprince, S., Berthier, E., Ayoub, F., Delacourt, C., & Avouac, J. P. (2008). Monitoring Earth surface dynamics with optical imagery. *EOS Transactions AGU*, *89*.

Leprince, S., Barbot, S., Ayoub, F., & Avouac, J. P. (2007a). Automatic and precise orthorectification, coregistration, and subpixel correlation of satellite images, application to ground deformation measurements, IEEE Trans. *Geoscience Remote Sensing*, *45*, 1529−1558.

Leprince, S., Ayoub, F., Klinger, Y., & Avouac, J. P. (2007b). Co-Registration of Optically Sensed Images and Correlation (COSI-Corr): An operational methodology for ground deformation measurements. *IEEE International Geoscience and Remote Sensing Symposium (IGARSS 2007), Barcelona*.

Long, J. T., & Sharp, R. P. (1964). Barchan dune movement in Imperial Valley, California. *Geological Society of America Bulletin*, *75*, 149−156.

Mann, D. H., Heiser, P. A., & Finney, B. P. (2002). Holocene history of the Great Kobuk Sand Dunes, northwest Alaska. *Quaternary Science Reviews*, *21*, 709−731.

McGowan, H. A., Petherick, L. M., & Kamber, B. S. (2008). Aeolian sedimentation and climate variability during the late quaternary in southeast Queensland, Australia. *Palaeogeography, Palaeoclimatology, Palaeoecology*, *265*, 171−181.

Meikle, H. D. (2001). *Modern radar systems.* Norwood, Massachusetts: Artech House.

Muhs, D. R. (1985). Age and paleoclimatic significance of Holocene dune sand in northeastern Colorado. *Annals of the Association of American Geographers*, *75*, 566−582.

Muhs, D. R., & Moat, P. B. (1993). The potential response of aeolian sands to greenhouse warming and precipitation reduction on the Great Plains of the USA. *Journal of Arid Environments*, *25*, 351−362.

Necsoiu, M., Leprince, S., Dinwiddie, C., Hooper, D., & Walter, G. (2009). Recent migration rates of the Great Kobuk Sand Dunes, Alaska: Technologic and scientific implications for planetary dune systems. *Lunar and Planetary Science Conference XXXX, 23–27 March 2009, Abstract #2074, The Woodlands, Texas*.

Scherler, D., Leprince, S., & Strecker, M. R. (2008). Glacier-surface velocities in alpine terrain from optical satellite imagery — Accuracy improvement and quality assessment. *Remote Sensing of Environment*, *112*, 3806−3819.

Speirs, J. C., McGowan, H. A., & Neil, D. T. (2008). Meteorological controls on sand transport and dune morphology in a polar-desert: Victoria Valley, Antarctica. *Earth Surface Processes and Landforms*, *33*, 1875−1891.

Thomas, D. S. G. (1984). Ancient ergs of the former arid zones of Zimbabwe, Zambia and Angola. *Transactions of the Institute of British Geographers, NS*, *9*, 75−88.

Vermeesch, P., & Drake, N. (2008). Remotely sensed dune celerity and sand flux measurements of the world's fastest barchans (Bodele, Chad). *Geophysical Research Letters*, *35*, L24404.

Walker, J., & Barrie, J. V. (2006). Geomorphology and sea-level rise on one of Canada's most sensitive coasts: Northeast Graham Island, British Columbia. *Journal of Coastal Research*, *1*, 220−226.

Wells, G. L. (1983). Late-glacial circulation over central North America revealed by aeolian features. In F. A. Street-Perrott, M. Beran, & R. Ratcliffe (Eds.), *Variations in the global water budget* (pp. 317−330). Dordrecht: Reidel.

Yao, Z. Y., Wang, T., Han, Z. W., Zhang, W. M., & Zhao, A. G. (2007). Migration of sand dunes on the northern Alxa Plateau, Inner Mongolia, China. *Journal of Arid Environments*, *70*, 80−93.

Yizhaq, H., Ashkenazy, Y., & Tsoar, H. (2009). Sand dune dynamics and climate change: A modeling approach. *Journal of Geophysical Research—Earth Surface*, *114*, F01023.